2017

Enhanced corrosion and wear resistance properties of carbon fiber reinforced Ni-based composite coating by laser cladding

Jianbo Lei

Chuan Shi

Shenfeng Zhou

Zhenjie Gu

Laichang Zhang
Edith Cowan University

10.1016/j.surfcoat.2017.11.051
This is an Author's Accepted Manuscript of:
Lei, J., Shi, C., Zhou, S., Gu, Z., & Zhang, L.C. (2018). Enhanced corrosion and wear resistance properties of carbon fiber reinforced ni-based composite coating by laser cladding. *Surface and Coatings Technology, 334*, 274-285.
https://doi.org/10.1016/j.surfcoat.2017.11.051

Enhanced corrosion and wear resistance properties of carbon fiber reinforced Ni-based composite coating by laser cladding

Jianbo Lei, Chuan Shi, Shengfeng Zhou, Zhenjie Gu, Lai-Chang Zhang

PII: S0257-8972(17)31198-2
DOI: doi:10.1016/j.surfcoat.2017.11.051
Reference: SCT 22899

To appear in: *Surface & Coatings Technology*

Received date: 17 July 2017
Revised date: 10 November 2017
Accepted date: 17 November 2017

Please cite this article as: Jianbo Lei, Chuan Shi, Shengfeng Zhou, Zhenjie Gu, Lai-Chang Zhang , Enhanced corrosion and wear resistance properties of carbon fiber reinforced Ni-based composite coating by laser cladding. The address for the corresponding author was captured as affiliation for all authors. Please check if appropriate. Sct(2017), doi:10.1016/j.surfcoat.2017.11.051

Enhanced corrosion and wear resistance properties of carbon fiber reinforced Ni-based composite coating by laser cladding

Jianbo Lei[a,*], Chuan Shi[a], Shengfeng Zhou[a,*], Zhenjie Gu[a], Lai-Chang Zhang[b,*]

[a]Laser Technology Institute, Tianjin Polytechnic University, Tianjin, 300387, China

[b]School of Engineering, Edith Cowan University, 270 Joondalup Drive, Joondalup, Perth, WA 6027, Australia

Abstract: To enhance the wear resistance and corrosion resistance of Ni-based coatings, carbon fibers reinforced nickel-based composite coatings (CFs/Ni) were fabricated on the surface of 1Cr13 stainless steel by laser cladding (LC). The microstructure characteristics, microhardness, wear and corrosion performances of the composite coatings were investigated. The results show that CFs can effectively improve the corrosion and wear resistances of Ni-based coatings. With increasing laser scanning speed, the morphology of CFs in composite coatings is more integral and the corrosion

* Corresponding author. Tel.: +86-22-83956392

E-mail address: ljbtj@163.com (J. Lei); zhousf1228@163.com(S. Zhou); lczhangimr@gmail.com; l.zhang@ecu.edu.au (L.C. Zhang)

and wear resistances of the composite coatings are improved. Especially, when laser scanning speed is increased to 8 mm/s, the average microhardness of the composite coating reaches up to 405 $HV_{0.2}$, which is about 1.3 times higher than that of Ni-based coating. Moreover, the corrosion current density and the wear rate of the composite coating are only 7% and 55% of those of the Ni-based coating, respectively, which is attributed to the good properties and homogeneous distribution of CFs and finer microstructure of composite coating.

Keywords: Laser cladding (LC); Carbon fibers; Nickel based coating; Electrochemical corrosion; Wear mechanisms

1. Introduction

Generally, Ni-based coatings exhibit excellent high-temperature oxidation and high-temperature wear performances so that they are usually applied in the field of bearings, engines, piston rods and at some high temperature environments [1]. The main methods for preparing Ni-based coatings are usually electroplating, thermal spraying (such as plasma spraying, flame spraying and arc spraying) [2-5]. For

electroplating, although the process is matured and the processing cost is relatively low, the process has some disadvantages. For example, electroplating coatings are very thin and the interface between coating and substrate is so poor that the electroplating coatings are susceptible to being peeled off from substrate during service. For thermal spraying, it has relatively higher efficiency, but the sprayed coatings are mechanically bonded to substrate and contain many pores and micro-cracks, resulting in premature failure therefore a decrease in service time [6, 7].

The continuing development of high-power lasers, computers and robots has made the metal laser additive manufacturing (i.e. metal 3D printing) become one of the hot spots, because it possesses many advantages as follows [8-12]. First, it can form complex structures and high-performance metallic components. Second, it can be applied to process metals with high melting point, such as Ti, Mo, W. Third, it is flexible to manipulate the local composition/microstructure of metallic components to achieve different performance requirements. Laser cladding (LC) is one kind of laser additive manufacturing and also has these aforementioned advantages. Therefore, it is one of the most advantageous processes for preparing the different key components.

However, the poor wear and corrosion resistances of Ni-based coatings fabricated by LC limits their wide applications in harsh environments. In order to avoid such disadvantages, adding alloy elements (such as Cr, W, Mo), rare earth oxides (such as Y_2O_3, CeO_2, La_2O_3) or secondary reinforcing phases (such as SiC, WC, B_4C, TiC) are usually adopted to further improve the wear and corrosion resistances of Ni-based coatings fabricated by LC [13-16]. Moreover, improving the process of LC, such as laser induction hybrid cladding [17], is also another way to strength the properties of Ni-based coatings, but the device is complicated.

Although the hardness and wear resistance of Ni-based coatings can be further improved via adding carbide particles such as WC, TiC and SiC into nickel matrix during LC, there also exist some defects in the resultant components. For example, stress concentration is caused by particles sharpness; plastic and toughness of coatings are decreased due to particle dissolution at high temperature molten pool. Regarding the alloyed method, it can not only improve the wear and corrosion resistances of Ni-based coatings, but also enhance the strength and toughness of Ni-based coatings simultaneously. However, the alloyed method has relatively high cost and some rare-

earth elements are highly toxic.

As such, extensive endeavors have been made to search for other reinforcing phases possessing better properties than those carbide particles, such as graphite, carbon nanotubes (CNTs) and carbon fibers (CFs). Lin et al. [18] added 2 wt.% graphene powders into Fe-based powder then fabricated the composite coatings by laser sintering. The results showed that the tensile strength and fatigue life of graphene reinforced Fe-based composite coatings are greatly improved compared with those for Fe-based coatings. Hwang et al. [19] found that CNTs is more stable than graphite in laser cladding process. In other words, graphite is easier to dissolve in the molten pool of laser cladding. Zhou et al. [20] fabricated the Cu-based composite coatings containing 2.6 wt.% CNTs on the surface of copper substrate by laser-induction hybrid cladding and found that the thermal conductivity and wear resistance of composite coatings can be enhanced simultaneously. Chen et al. [9] prepared CNTs reinforced Ni-based superalloy coatings by laser powder deposition. It was found that, although the mechanical properties of composite coatings are enhanced, a lot of CNTs are dissolute and deformed. In addition, Suarez et al. [21] found that CNTs tend to agglomerate due

to van der Waals forces, thereby significantly reducing the enhancement effect for the coating.

In general, CFs possess high temperature oxidation resistance and good corrosion resistance as well as self-lubricate property, which can significantly reduce the friction coefficient of coatings. In particular, the short CFs are easy to be distributed homogeneously in composites, resulting in isotropic mechanical properties of the short CFs reinforced composites. Although there exist some studies on the mechanical properties and wear resistance of CFs reinforced nickel matrix composites by powder metallurgy and hot isostatic pressing (HIP) [22, 23], they were mainly focused on the bulk composites. There is still no study on the corrosion mechanism and wear mechanism of CFs/Ni-based coatings by LC. As such, the main objective of this work is to study the processing of CFs/Ni-based coatings by LC at different laser scanning speed and the CFs morphology, electrochemical corrosion and wear mechanisms of the LC-produced composite coatings.

2. Experimental

2.1 Raw materials used

The substrate material used in this work was 1Cr13 stainless steel with the dimension of 100mm×60mm×10mm. The chemical composition of 1Cr13 stainless steel was listed in Table 1. The bonding metal was Ni25, with its chemical composition listed in Table 2. The CFs with 6 μm in diameter and 40 μm long were used as the reinforcement phase. Before LC, CFs were heated in a resistance furnace at 573 K for 30 min to remove the glues on the surface. Then CFs and Ni25 alloy powder were mixed in planetary ball mill (TJ-2L, China) with the powder to ball mass ratio of 1:4 at the speed of 300 rpm for 4 h. Stainless steel balls (4 mm in diameter) and milling vessels were used. In addition, ethanol was also used as the solvent. The volume fraction of CFs added to the composite was 6 vol.%. The morphology of the composite powder after milling and the distribution of raw powder were shown in Fig. 1. The equivalent diameter of CFs was approximately 6 μm and its length was about 40 μm, which were kept the same as for the raw CFs.

2.2 LC parameters

The LASERTEL 8 kW high power semiconductor laser with a wavelength of 980 nm and the spot size of 12 mm×3 mm was used. Single tracks of the coating with a thickness of 2 mm was deposited by the preplaced powder method. A shielding of Argon gas was used to protect the molten pool. The schematic drawing of LC was described in Fig. 2. The laser power was 3.2 kW and the laser scanning speeds used were 2, 5, and 8 mm/s, respectively.

2.3 Microstructure characterization

After LC, the specimens were mechanically grounded, polished, and etched by a solution of 90% alcohol (analytical reagent) and 10% HNO_3 (analytical reagent). The microstructure characteristics, fiber distribution and elements distribution of composite coatings were analyzed by ZEISS Sigma 300 field emission scanning electron microscopy (SEM) equipped with X-ray energy-dispersive spectrometer (EDS) at an accelerating voltage of 20 kV. A D/MAX-2500 X-ray diffraction (XRD) machine was used to analyze the phases of coatings (Cu target, 40 kV, 140 mA). Tecnai GF20 field emission transmission electron microscopy (TEM) was adopted to analysis the

morphology of CFs within coatings.

2.4 Properties evaluation

Microhardness distribution of composite coatings was measured by using a HV-1000 Vickers digital microhardness tester with a load of 1.96 N and a dwell time of 15s. To investigate the effect of laser scanning speed and CFs addition on the corrosion resistance of composite coatings, the electrochemical resistance in 3.5 wt.% NaCl solution was measured by the CHI604e electrochemical analyzer (Chenhua, Shanghai). A three-electrode cell was used for the measurements, where a saturated calomel electrode (SCE) was used as the reference electrode and a platinum foil (Pt) was used as the counterpart. The specimens with an exposed area of about 1 cm^2 as the working electrode. All specimens were immersed in the test electrolyte at room temperature for 1 h to stabilize the open circuit potential (OCP). The potentiodynamic polarization scanning was varied from –0.95 V to +0.2 V, and the sweep rate was 5 mV/s. The corresponding corrosion current density (i_{corr}) and corrosion potential (E_{corr}) were determined using the Tafel extrapolation method. Electrochemical impedance

spectroscopy (EIS) tests were performed at the OCP with an AC amplitude of 10 mV in the frequency range from 10^5 Hz to 10^{-2} Hz.

Friction and wear experiments were conducted in air using a block-on-ring wear test machine (M-2000) at room temperature. The size of the block was 12 mm×10 mm×10 mm, and the counterpart ring with 40 mm in outside diameter and 10 mm in thickness was made of GCr15 bearing steel with the hardness of HRC 60±2. Meanwhile, the tests were carried out under the dry sliding condition and the applied load was maintained at 250 N. Moreover, three samples for each laser scanning speed were tested, from which all the reported properties were averaged in this work. The ring was rotated at 300 rpm for 8 h. After the wear tests, the debris and worn surfaces were analyzed by SEM and EDS.

3. Results and discussion

3.1 Microstructure characteristics of composite coatings

Fig. 3 shows the XRD patterns for the Ni-based coating and CFs/Ni coatings. The composite coatings are mainly composed of γ-(Ni, Fe), CFs, carbides such as $M_{23}C_6$,

M_7C_3, $Fe_4C_{0.63}$ and Ni_3B, suggesting that laser scanning speed has no significant effect on the phase constituent of the composite coatings.

The microstructure of CFs/Ni and Ni-based coatings are shown in Fig. 4. It can be seen that the microstructure characteristics of composite coatings from bonding zone to the top coating are mainly planar crystal, cellular crystals, columnar dendrites and equiaxed crystals. With increasing laser scanning speed, the thickness of planar crystal is reduced from 17.2μm at 2 mm/s to 4.7μm at 5 mm/s (Figs. 4a~c), the columnar dendrites present an elongated morphology and the secondary dendrites are refined gradually. When laser scanning speed is further increased to 8 mm/s, the columnar dendrites in bonding zone and central region are further reduced. However, the amount of the refined cellular crystals is increased (Figs.4e~g), while the equiaxed crystals near the top coating are refined (Figs.4i~k) from 17.7μm at 2 mm/s to 7.2μm at 8 mm/s. However, when the processing parameters are constant, the CFs/Ni-based coatings display much finer microstructure than Ni-based coatings (Figs. 4d, 4h and 4l), which indicates that CFs are beneficial to refine grains.

According to rapid solidification theory, the morphology in the microstructure of

coatings is mainly dependent on the extent of constitutional undercooling, which is closely related to the solidification velocity (R) and the temperature gradient (G). The relationship can be expressed by the following equation: [24, 25]

$$G = \frac{2k(T - T_0)^2}{\varepsilon P} \tag{1}$$

$$R = V_s \cos\theta \tag{2}$$

where T is the liquid temperature of the alloy, T_0 is the initial temperature of the substrate, ε is the absorption coefficient of the laser, P is the laser power, k is the thermal conductivity of coating, V_s is the laser scanning speed, and θ is the angle between V_s and R.

The primary dendrite arm spacing can be described as follows [26]:

$$\lambda = \frac{a}{\sqrt{GR}} \tag{3}$$

where a is the coefficient. Manipulations of the Eqs. (1), (2) and (3) lead to the following equation.

$$\lambda = \frac{a\sqrt{\varepsilon P}}{(T - T_0)\sqrt{2kV_s \cos\theta}} \tag{4}$$

In the melting zone of substrate, the temperature gradient G in front of the solid-liquid interface is very large and the extent of constitutional undercooling is small. As

such, the molten metal near the bonding line is in the form of planar crystal and grows up from the bottom of the molten pool. With increasing the distance from the bonding line, the temperature gradient decreases. So, the solid/liquid interface of the planar crystal becomes unstable when constitutional undercooling is greater than the front solidification speed, resulting in that the planar crystal is transformed into the cellular crystals and dendrites. At the bottom of molten pool, the growth of microstructure tends to along the largest direction of thermal flux density. As a result, the growth of the cellular crystals and dendrites near the bonding zone is perpendicular to the planar crystal, because the heat is mainly transmitted from molten pool to the substrate during LC. In the areas near the surface of molten pool, the growth of microstructure is changed from columnar dendrites to equiaxed crystals, which is attributed to heat transmission to the surrounding environment from multiple directions. With increasing laser scanning speed, the solidification rate R increases therefore the ratio G/R decreases. As a result, the morphology of microstructure is transformed from planar crystals to cellular crystals and dendrites rapidly. According to the Eq. (4), when laser scanning speed increases, the value of the λ decreases, indicating that the grains

are refined. Therefore, the thickness of the planar crystals decreases gradually. The number of the dendrites is decreased and the refined cellular crystals are increased with increasing laser scanning speed.

3.2 Characteristics of carbon fibers

Fig. 5 shows the distribution characteristics of CFs in the composite coatings fabricated by LC. It can be seen that CFs are mainly distributed at grain boundaries. Similar distribution characteristic of CFs was also reported in CFs/Mg composites by powder metallurgy [27]. In addition, CFs are distributed more and more homogeneously with increasing laser scanning speed, and the morphology of CFs displays a more regular circle in the composite coatings when laser scanning speed is increased to 8 mm/s. While laser scanning speed is only 2 mm/s, a large number of dark particles are distributed along grain boundaries (Fig. 5a). According to the EDS analysis, point A is composed of 35.8% C, 23.8% Fe, 34.5% Ni, 4.5% Cr and 1.4% Si (all in wt.%), indicating these black particles are CFs that have been dissolved and interacted with alloys to form carbides. When laser scanning speed is increased to 5 mm/s, the

dark phases that distributed along grain boundaries are reduced, whereas the cross-sectional morphology of CFs is deformed and displayed complex thin stripes, shown as white arrows pointed (Fig. 5b). When laser scanning speed is further increased to 8 mm/s, little dark particles can be found along grain boundaries. The cross-sectional morphology of CFs in the composite coatings are relatively regular, and the distribution of CFs along the grain boundaries is homogenous. Moreover, there is no obvious segregation between CFs (Fig. 5c). Fig. 5d shows the typical morphology of CFs with lamellar structure, suggesting that the structure of CFs is basically well preserved. In addition, no gaps or cracks can be found in the interface of carbon fiber and Ni-based matrix. Fig. 6 shows the element distribution of the lineal energy spectrum. C element is mainly distributed in the carbon fibers and little diffuses outward. But at the interface of CF and matrix, elements such as Cr, Fe, Ni and Si are diffused into the carbon fiber slightly, suggesting that CFs are kept the integrity of structure and a good interface bonding when laser scanning speed is relatively higher.

It is well known that the center region of the laser beam with a Gaussian distribution has the highest intensity. As a result, there exists a temperature gradient in

the radial direction on the surface of molten pool. Such a temperature gradient would raise the surface tension gradient, thereby causing the materials near the surface of molten pool flow from center to edges. As such, materials at the edge flow along the solid line under the action of shearing force, then the melt flow encounters at the bottom of the pool and rises to the surface, forming Marangoni convection [28]. Generally, material transfer is mainly dependent on the convection in laser molten pool [29]. Under the role of Marangoni convection, short CFs continue moving to the surface of molten pool, so as to suffer from the high-energy laser beam ablation and destruction. When a low laser scanning speed is adopted during LC, the solidification rate is low. Thus, the time of CFs subjected to thermal damage of laser beam is longer, and most CFs are burned during the floating process (Fig. 7a), thereby weakening the reinforcement effect of CFs. When laser scanning speed is increased to 8 mm/s, the laser specific energy is reduced and the solidification rate R increases. Thus, the time of CFs subjected to laser beam is reduced during LC and the morphology of CFs remains integrity (Fig. 7b). From thermodynamic point of view, the criterion for judging materials that can be captured by the front of solid-liquid interface is explained as

follows [30]:

$$\frac{K_C}{K_{Ni}} > 1 \tag{5}$$

$$\left(\frac{K_C C_C \rho_C}{K_{Ni} C_{Ni} \rho_{Ni}}\right)^{\frac{1}{2}} > 1 \tag{6}$$

where K_C and K_{Ni} are the thermal conductivity of carbon fiber and Ni, respectively; C_C and C_{Ni} are the specific heat capacity of carbon fiber and Ni, respectively; ρ_C and ρ_{Ni} represent the density of carbon fiber and Ni, respectively. When $K_C/K_{Ni}<1$, single carbon fiber plays a role in heat insulation at the solid-liquid interface. The solidified interface behind carbon fiber forms a raised surface so that carbon fiber is expelled by solid-liquid (S/L) interface due to the effect of interface curvature. On the contrary, if $K_C/K_{Ni}>1$, the trough that forms at the S/L interface will engulf the CFs. According to the Eqs. (5), (6) and Table 3 [31], $K_C/K_{Ni}=0.16<1$, $(K_C C_C \rho_C/K_{Ni} C_{Ni} \rho_{Ni})^{1/2}=0.22<1$, thus CFs are expelled by solid-liquid interface during rapid solidification. Furthermore, there exist many dislocations and vacancies around the grain boundaries of Ni-based metallic matrix due to the structural stress caused by the volume shrinkage and phase transformation after rapid solidification. The CFs tend to be distributed at these defects to reduce interfacial energy around the grain boundaries. As a result, most CFs are

distributed homogeneously around grain boundaries. Due to Zener Pinning effect [32], CFs increase the frictional resistance for the movement of grain boundaries, inhibit the grain growth and finally result in grain refinement. Furthermore, with increasing laser scanning speed, CFs that are distributed evenly along the grain boundaries with less burned and deformed further play an effective role in suppressing grain growth.

3.3 Microhardness characteristics of composite coatings

Fig. 8 shows the microhardness distribution of composite coatings. It can be seen from Fig. 8a that microhardness of CFs/Ni-based coating is approximately 1.3 times higher than that of Ni-based coatings, indicating that CFs can evidently enhance the microhardness of composite coatings. The average microhardness of CFs/Ni coatings increases with an increase in laser scanning speed (Fig. 8b).

It can be seen from Fig. 8c that $d^{-1/2}$ has a linear relationship with microhardness, which suggests that the relationship between the microhardness and grain size (d) satisfies the classical Hall-Petch equation [33-35]. With increasing laser scanning speed, the microhardness increases, which can be explained by the Hall-Petch effect. Namely,

the increased laser scanning speed improves the degree of grain refinement (Fig. 4), which makes the grain boundaries much more than the original grain boundaries. As a result, the external force that requires to produce the dislocation pile-up increases. So, the microhardness of the coatings is enhanced.

3.4 Electrochemical performance of composite coatings

Fig. 9 shows the results of electrochemical experiments. It can be seen from the anodic polarization curves (Fig. 9a) that all coatings have passivation regions, indicating that the corrosion process has a passivation behavior. The lowest corrosion current density of CFs/Ni coatings (1.663×10^{-6} A/cm^2) is 7% that of Ni-based coating (2.350×10^{-5} A/cm^2). However, the lowest passivation current density of CFs/Ni coatings (3.844×10^{-6} A/cm^2) is only 6 % that of Ni-based coating (6.491×10^{-5} A/cm^2) and the highest polarization resistance of CFs/Ni coatings (25.350 kΩ/cm^2) is about 4.4 times higher than that of Ni-based alloy coating (5.746kΩ/cm^2) (Table 4), indicating that CFs can improve the corrosion resistance of Ni-based coating. For CFs/Ni coatings, the corrosion current densities i_{corr} and the passivation current densities i_{pass} show a decreasing trend with an increase in laser scanning speed. Moreover, the polarization

resistances R_p increases, suggesting that the increase in laser scanning speed can improve the electrochemical corrosion resistance of CFs/Ni coatings.

It can be seen from Nyquist plots (Fig. 9b) that the radii of the capacitive impedance loops of CFs/Ni coatings are greater than that of Ni-based coating. Moreover, the radii of the capacitive impedance loops of CFs/Ni coatings become greater with increasing laser scanning speed. As well known, the larger the radius of the capacitive impedance loop is, the better is the corrosion resistance [36]. Thus, CFs can largely improve the corrosion resistance of composite coatings. Generally, the ability of inhibiting the penetration of electrolyte in the composite coatings is related to the middle frequency loop [37]. The larger the middle frequency loop is, the better is the corrosion resistance. When laser scanning speed are 5 mm/s and 8 mm/s, the middle frequency loops are obviously larger than the others in Bode curves (Fig. 9c), indicating that the corrosion resistance of the two kinds of composite coatings are better than that of the others. Moreover, the values of $|Z|_{0.01Hz}$ increase gradually (Fig. 9d) with an increase in laser scanning speed, showing that the composite coatings can serve as more effective barrier layer with corrosion when laser scanning speed is increased [38, 39].

In conclusion, the EIS results further confirm that CFs can enhance the corrosion resistance of Ni-based coatings, and the corrosion resistance of CFs/Ni coatings increases with increasing laser scanning speed.

The electrochemical corrosion reactions of M (Ni, Cr) in 3.5 wt.% NaCl solution at room temperature are as follows:

$$M \rightarrow M^{+} + e^{-} \text{ (anodic reaction)} \quad (7)$$

$$2H_2O + O_2 + 4e^{-} \rightarrow 4OH^{-} \text{ (cathodic reaction)} \quad (8)$$

The final products can be written as the following reactions:

$$M^{+} + OH^{-} \rightarrow M(OH) \quad (9)$$

$$M(OH) + OH^{-} \rightarrow MO + H_2O \quad (10)$$

Then the passivation film is broken by Cl^- within the electrolyte:

$$MO + 2Cl^{-} + H_2O \rightarrow MCl_2 + 2OH^{-} \quad (11)$$

Fig. 10 shows the morphology of Ni-based coating and CFs/Ni coatings after corrosion tests. The prominent corrosion occurs around the grain boundaries of γ-Ni (Fig. 10a). It can be explained by the following reasons. Those C atoms adjacent to grain boundaries are prone to interact with Cr to form $M_{23}C_6$ and M_7C_3 carbides,

thereby decreasing the Cr content at boundaries and forming Cr-depleted regions at grain boundaries [40]. As a result, the corrosion resistance of grain boundaries decreases and the preferential corrosion takes place. Compared with C element, CFs are chemical inertness and much more stable at high temperature [23]. Namely, C element is easier to form carbides with alloying elements at high temperature. CFs are distributed homogeneously along grain boundaries so that CFs can squeeze into the positions of the defects at the grain boundaries, which can reduce segregation amount of M_7C_3 and $M_{23}C_6$ carbides. Moreover, CFs have much better corrosion resistance than the M_7C_3 and $M_{23}C_6$ carbides, which in turn can reduce the degree of corrosion. Hence, the internal defects of the composite coatings are reduced and the density of the carbides near grain boundaries is also decreased. Cr atoms in solid solution in grains are evenly distributed around CFs, thereby improving the corrosion resistance near grain boundaries. In addition, the refined grains have more grain boundaries, thereby increasing the diffusion rate of Cr to form the passivation films rapidly so that the corrosion process is inhibited [41]. For Ni-based coating without CFs, M_7C_3 and $M_{23}C_6$carbides are segregated along grain boundaries, resulting in higher activity of

grain boundaries during electrochemical measurement. Therefore, grain boundaries and grains tend to form smaller anode or greater cathode micro-batteries to accelerate the intergranular corrosion [42]. For CFs/Ni coating, the potential difference between CFs and grains near grain boundaries is decreased because the potential of CFs is much higher than that of carbides [43]. As a result, the corrosion resistance of the composite coatings is improved. However, when the laser scanning speed is only 2 mm/s, CFs cannot maintain the original structure but they are seriously damaged and interact with Ni-based matrix to form the carbides distributed at grain boundaries (Fig. 5a), resulting in poor corrosion resistance. When the laser scanning speed is increased to 8 mm/s, the structure of CFs is well kept and CFs are distributed homogeneously in Ni-based coatings (Figs. 5c and 5d). In addition, the grain boundaries of Ni-based composite coatings are much cleaner and few M_7C_3 and $M_{23}C_6$ carbides can be found in these areas (Fig. 11). This indicates that CFs with few defects can decrease the amount of M_7C_3 and $M_{23}C_6$ carbides at grain boundaries, so that the corrosion resistance of Ni-based alloy composite coatings is improved significantly.

3.5 Wear properties of composite coatings

Fig. 12 shows the results of friction and wear tests for Ni-based coating and CFs/Ni coatings. Both the friction coefficient and wear rate decrease with increasing laser scanning speed, as shown in Figs. 12a and 12b. Especially, when the laser scanning speed is increased to 8 mm/s, the lowest wear rate of Ni-based composite coatings (0.00208 mg/m) is just 55% of Ni-based coating (0.00375 mg/m). This indicates that CFs can significantly reduce the friction coefficient and wear rate of Ni-based coating. Thus, the wear resistance of composite coatings is improved.

Fig. 13 shows the morphology of the debris. According to the EDS analysis (Table 5), the contents of Fe and O are higher than other elements in the debris, suggesting that the debris is mainly from the ring and is oxidized by air to form iron oxidation during the friction process. In addition, there exist some Ni and Cr elements in the debris. This is attributed to that Ni, Cr elements are easy to diffuse into the debris during the friction process. Under the same processing parameters, the size of debris of CFs reinforced Ni-base composite coatings is smaller (1.14μm) compared with that of Ni-based coating (2.81μm) (Figs. 13a and 13d). Meanwhile, the debris of composite

coatings is refined gradually with an increase in laser scanning speed (Figs.13b~13d).

Fig. 14 shows the morphology of the worn surface after dry sliding wear. The wear degree for the composite coatings is significantly lower than that of Ni-based coating without CFs reinforcement (Figs. 14a and 14d). As shown in Figs.14a and 14b, the debris is pushed into the spalling pits and evident phenomenon for material transfer is observed on the surface of coating, indicating that adhesive wear behavior occurs during the wear process. Some dark and sheet-like materials on the worn surfaces of the coatings (such as point E, F) are observed in Figs. 14b and 14c, which are mainly iron oxidation according to the EDS analysis (Table 5). With increasing the laser scanning speed, the adhesive materials on the worn surface are reduced and the spalling pits are also reduced, showing that the wear resistance of the composite coatings is relatively better (Figs. 14b~14d).

In the initial stage of the dry sliding wear, the ring is firstly contacted with bonding metal which is relatively soft. As a result, the adhesive wear takes place. With proceeding of the wear process, some debris falls from the surfaces of ring and coating and is transmitted to the secondary abrasive particles under the action of friction force,

resulting in plastic deformation and features of plowing grooves. This indicates that the abrasive wear has taken place. On one hand, during the dry sliding wear, the friction force acting on the surface of coating causes the plastic deformation of subsurface, which keeps on accumulating with repeated load. When the plastic deformation reaches a certain degree, the cracks nucleation occurs in the subsurface and continues propagating to the surface. On the other hand, the friction heat causes the temperature rising, so that the contact surface between ring and coating becomes relatively soft. The abrasive wear aggravates on the friction surface. Thus, the debris on the friction surface increases, which forms more obviously micro-cutting. Due to the micro-cutting of abrasive particles and crack propagation, the fragments are peeled off from the surface of coating (Fig. 13b).

For CFs/Ni coatings, CFs have good self-lubricate property and are in the form of graphite particles or segments which pressed and adhered to the surface of the composite coatings to form a lubricating layer during dry sliding wear [44]. The lubricating layer can reduce the direct contact between ring and composite coating, so that the friction coefficient and wear rate of the composite coatings are decreased [45].

Due to the thermal conductivity of GCr15 (36.92 W/(K·m)) is relatively poor compared with the composite coatings, the hardness of the surface of GCr15 decreases sharply. Therefore, the materials on the surface of the ring begin to transfer to the surface of the composite coating. However, the materials that transferred from the ring took place plastic deformation after a number of repeated rolling, so that ultimately many dark and sheet-like materials are formed on the surface of the composite coating. When the laser scanning speed is low, a lot of CFs suffer from dissolution and heat damage, M_7C_3 and $M_{23}C_6$ carbides precipitated in the composite coating are increased (Fig. 5a). As a result, the abrasive particles increase during dry sliding wear, so that the micro-cutting is obvious. In addition, the cracks are easy to propagate because the precipitated carbides in the coating can increase the brittleness of the coating, resulting in large debris peeled off from the surface. With increasing laser scanning speed, the degree of dissolution and heat damage of CFs decreases, so the content of the precipitated carbides decreases, and the surface of the composite coating mainly suffers from the abrasive wear. Because many CFs are not dissolved completely, so that they can prevent the wear from further aggravation. As a result, the friction coefficient and the wear rate of the composite

coating are decreased. When the laser scanning speed is higher, CFs are distributed more homogeneously and shapes are more regular than those in other coatings. Thus, a uniform and good lubricating layer is formed constantly during dry sliding wear, and the wear mechanism of surface is dominated by abrasive wear. Furthermore, the microhardness of the composite coating is the highest so that the abrasive particles are not easy to pierce into the surface to cause micro-cutting, therefore the wear resistance of the composite coating is improved.

CFs with good combination of interfaces can effectively transmit the load from friction surface to Ni-based matrix, which can enhance the resistance to plastic deformation of the subsurface [46]. This is also the main reason why peeling does not occur when laser scanning speed are 5 mm/s and 8 mm/s. In other words, CFs can effectively inhibit the propagation of the cracks and improve the strength of the composite coating as well as the resistance to plastic deformation of the subsurface. As a result, the wear resistance of CFs/Ni coating is improved.

3.6 Residual stress

Generally, the composite coatings fabricated by laser cladding are vulnerable to crack due to the residual stress in the coatings. The residual stress is composed of the contraction stress σ_{vol} and the thermal stress σ_T. The thermal stress can be explained as follows [47]:

$$\sigma_T = \frac{E_c E_s t_s (\alpha_c - \alpha_s)\Delta T}{(1-V)(E_s t_s + E_c t_c)} \tag{12}$$

where E_c and E_s are elastic modulus of the coating and the substrate, respectively; t_c and t_s are the height of the coating and substrate, respectively; α_c and α_s are the coefficient of thermal expansion (CTE) of the coating and substrate, respectively; V represents Poisson ratio; and ΔT is the difference between the solidification temperature of the molten cladding material and the room temperature. Zhou [48] et. al studied the residual stress of Ni-based WC composite coatings fabricated by LC. It is found that crack sensitivity increases with increasing laser scanning speed. However, in this work, with increasing laser scanning speed, there is no apparent micro-cracks in CFs/Ni-based coatings. The reasons are discussed in the following. When the temperature of composite coating gradually recovers to room temperature, metal in the matrix shrinks (CTE of Ni25 is about 13.3-16.8×10^{-6} K^{-1}). However, due to the negative CTE of CFs

(about -0.74×10^{-6} K^{-1} in axial direction), CFs would expand instead. When laser scanning speed is high, CFs are distributed uniformly and with good morphology in the coating as well as good interfacial bonding, which can impel the expansive CFs to restrict the metal contracting. As a result, the convection stress is significantly reduced. Also, a better interfacial bonding between CFs and the matrix can lead to a stronger physical confinement thereby lowering the CTE of the composite [49]. According to Eq. (12), the thermal stress σ_T may reduce because of the reduction in CTE of the coating (α_c). Besides, with increasing the laser scanning speed, many columnar crystals transform into refined cellular crystals and equiaxed crystals, as discussed in Section 3.1. The fine equiaxed crystals can be easily to realize the coordinated deformation between the grains, so that these fine equiaxed crystals can well adjust the convection stress [50].

To sum up the discussion above, with increasing laser scanning speed, because of negative CTE of CFs and finer equiaxed crystals as well as good interfacial bonding, the convection stress and thermal stress of CFs/Ni-based coating may be reduced. Therefore, the residual stress is reduced and the CFs/Ni-based coatings fabricated by

LC are free of cracks. The further experiments and discussions will be reported in the near future.

4. Conclusions

In the present work, CFs/Ni-based coatings are successfully fabricated by LC without prominent micro-cracks. It is found that CFs and laser scanning speed have an important positive influence on the microstructure characteristics and performances of the composite coatings. With an increase in laser scanning speed, CFs dispersion and morphology are better than those at low laser scanning speed. So the refinement of grains is more apparent, thereby enhancing the properties of the composite coating. The main conclusions are drawn as follows.

1.When laser scanning speed is 8 mm/s, the CFs/Ni-based composite coating has a refined microstructure and good dispersion of CFs in the microstructure. As such, the CFs/Ni-based composite coating exhibit high performance in terms of microhardness, corrosion resistance and wear resistance.

2.Compared with Ni-based coating, the corrosion resistance of CFs/Ni coatings is

relatively higher. With increasing the laser scanning speed, the corrosion resistance of CFs/Ni-based coatings gradually increases due to high corrosion resistance of CFs and decrease in the amount of precipitated M_7C_3 and $M_{23}C_6$ carbides adjacent to grain boundaries.

3. CFs/Ni-based coatings show better wear resistance than Ni-based alloy coatings. With an increase in laser scanning speed, the wear resistance of the composite coatings gradually increases, which can be attributed to good self-lubrication property and good dispersion of CFs in the coatings.

Acknowledgments

This work was financially supported by the National Natural Science Foundation of China (Grant No. 61475117, 51471084), Applied Basic Research and Development Project of Tianjin City (Grant No.12JCQNJC02800), the Key Technology R & D Program of Tianjin City (Grant No. 13ZCZDGX01109), the Foundation of Civil Aviation University of China (Grant No. 2014TJPUJG), the Science and Development Foundation of Higher Education Institutions of Tianjin City (Grant No. 20120631), and

the Outstanding Youth Foundation of Jiangxi Province (Grant No.20162BCB23039).

References

[1] J. Xu, L. Zhao, X. Deng, H. Yu, High temperature simulation of short carbon fiber-reinforced nickel base composite, Materials & Design 27(10) (2006) 1152-1156.

[2] N. Elkhoshkhany, A. Hafnway, A. Khaled, Electrodeposition and corrosion behavior of nano-structured Ni-WC and Ni-Co-WC composite coating, Journal of Alloys and Compounds 695 (2017) 1505-1514.

[3] A. Chaudhuri, Y. Raghupathy, D. Srinivasan, S. Suwas, C. Srivastava, Microstructural evolution of cold-sprayed Inconel 625 superalloy coatings on low alloy steel substrate, Acta Materialia 129 (2017) 11-25.

[4] G. Bolelli, A. Candeli, L. Lusvarghi, T. Manfredini, A. Denoirjean, S. Valette, A. Ravaux, E. Meillot, "Hybrid" plasma spraying of NiCrAlY+Al_2O_3+h-BN composite coatings for sliding wear applications, Wear 378-379 (2017) 68-81.

[5] L. He, Y. Tan, X. Wang, T. Xu, X. Hong, Microstructure and wear properties of Al_2O_3-CeO_2/Ni-base alloy composite coatings on aluminum alloys by plasma spray, Applied Surface Science 314 (2014) 760-767.

[6] J.J. Tian, S.W. Yao, X.T. Luo, C.X. Li, C.J. Li, An effective approach for creating metallurgical self-bonding in plasma-spraying of NiCr-Mo coating by designing shell-core-structured powders, Acta Materialia 110 (2016) 19-30.

[7] M. Jafari, M.H. Enayati, M. Salehi, S.M. Nahvi, C.G. Park, Microstructural and mechanical characterizations of a novel HVOF-sprayed WC-Co coating deposited from electroless Ni–P coated WC-12Co powders, Materials Science and Engineering: A 578 (2013) 46-53.

[8] Y.J. Liu, H.L. Wang, S.J. Li, S.G. Wang, W.J. Wang, W.T. Hou, Y.L. Hao, R. Yang, L.C. Zhang, Compressive and fatigue behavior of beta-type titanium porous structures fabricated by electron beam melting, Acta Materialia 126 (2017) 58-66.

[9] Y. Chen, F. Lu, K. Zhang, P. Nie, S.R. Elmi Hosseini, K. Feng, Z. Li, Laser powder deposition of carbon nanotube reinforced nickel-based superalloy Inconel 718, Carbon 107 (2016) 361-370.

[10] D.D. Gu, W. Meiners, K. Wissenbach, R. Poprawe, Laser additive manufacturing of metallic components: materials, processes and mechanisms, International Materials Reviews 57(3) (2013) 133-164.

[11] L.C. Zhang, H. Attar, Selective Laser Melting of Titanium Alloys and Titanium Matrix Composites for Biomedical Applications: A Review, Advanced Engineering Materials 18 (2016) 463-475.

[12] C.Y. Yap, C.K. Chua, Z.L. Dong, Z.H. Liu, D.Q. Zhang, L.E. Loh, S.L. Sing, Review of selective laser melting: Materials and applications, Applied Physics Reviews 2(4) (2015) 041101.

[13] M.M. Quazi, M.A. Fazal, A.S.M.A. Haseeb, F. Yusof, H.H. Masjuki, A. Arslan, Effect of rare earth elements and their oxides on tribo-mechanical performance of laser claddings: A review, Journal of Rare Earths 34(6) (2016) 549-564.

[14] Y. Cai, Z. Luo, M. Feng, Z. Liu, Z. Huang, Y. Zeng, The effect of TiC/Al2O3 composite ceramic reinforcement on tribological behavior of laser cladding Ni60 alloys coatings, Surface and Coatings Technology 291 (2016) 222-229.

[15] X. Luo, J. Li, G.J. Li, Effect of NiCrBSi content on microstructural evolution, cracking susceptibility and wear behaviors of laser cladding WC/Ni–NiCrBSi composite coatings, Journal of Alloys and Compounds 626 (2015) 102-111.

[16] Y. Zhao, J. Sun, J. Li, Effect of rare earth oxide on the properties of laser cladding

layer and machining vibration suppressing in side milling, Applied Surface Science 321 (2014) 387-395.

[17] Y. Huang, X. Zeng, Q. Hu, S. Zhou, Microstructure and interface interaction in laser induction hybrid cladding of Ni-based coating, Applied Surface Science 255(7) (2009) 3940-3945.

[18] D. Lin, C. Richard Liu, G.J. Cheng, Single-layer graphene oxide reinforced metal matrix composites by laser sintering: Microstructure and mechanical property enhancement, Acta Materialia 80 (2014) 183-193.

[19] J.Y. Hwang, A. Neira, T.W. Scharf, J. Tiley, R. Banerjee, Laser-deposited carbon nanotube reinforced nickel matrix composites, Scripta Materialia 59(5) (2008) 487-490.

[20] S. Zhou, C. Wu, T. Zhang, Z. Zhang, Carbon nanotube- and Fep-reinforced copper–matrix composites by laser induction hybrid rapid cladding, Scripta Materialia 76 (2014) 25-28.

[21] S. Suárez, E. Ramos-Moore, B. Lechthaler, F. Mücklich, Grain growth analysis of multiwalled carbon nanotube-reinforced bulk Ni composites, Carbon 70 (2014) 173-178.

[22] K. Shirvanimoghaddam, S.U. Hamim, M. Karbalaei Akbari, S.M. Fakhrhoseini, H. Khayyam, A.H. Pakseresht, E. Ghasali, M. Zabet, K.S. Munir, S. Jia, J.P. Davim, M. Naebe, Carbon fiber reinforced metal matrix composites: Fabrication processes and properties, Composites Part A: Applied Science and Manufacturing 92 (2017) 70-96.

[23] A. Khoddamzadeh, R. Liu, M. Liang, Q. Yang, Wear resistant carbon fiber reinforced Stellite alloy composites, Materials & Design (1980-2015) 56 (2014) 487-494.

[24] S. Zhou, Y. Huang, X. Zeng, Q. Hu, Microstructure characteristics of Ni-based WC composite coatings by laser induction hybrid rapid cladding, Materials Science and Engineering: A 480(1-2) (2008) 564-572.

[25] M. Zhong, W. Liu, K. Yao, J.-C. Goussain, C. Mayer, A. Becker, Microstructural evolution in high power laser cladding of Stellite 6+WC layers, Surface and Coatings Technology 157(2-3) (2002) 128-137.

[26] Y. Huang, X. Zeng, Q. Hu, S. Zhou, Microstructure and interface interaction in laser induction hybrid cladding of Ni-based coating, Applied Surface Science 255(7) (2009) 3940-3945.

[27] L.G. Hou, R.Z. Wu, X.D. Wang, J.H. Zhang, M.L. Zhang, A.P. Dong, B.D. Sun, Microstructure, mechanical properties and thermal conductivity of the short carbon fiber reinforced magnesium matrix composites, Journal of Alloys and Compounds 695 (2017) 2820-2826.

[28] B. Ma, J. Li, Z. Peng, G. Zhang, Structural morphologies of Cu–Sn–Bi immiscible alloys with varied compositions, Journal of Alloys and Compounds 535 (2012) 95-101.

[29] T.R. Anthony, H.E. Cline, Surface rippling induced by surface-tension gradients during laser surface melting and alloying, Journal of Applied Physics 48(9) (1977) 3888-3894.

[30] D.Stefanescu, Solidification of Metal Matrix Composites. In: Science and Engineering of Casting Solidification. Springer, Cham, 2015.

[31] Y. Liu, S. Kumar, Recent Progress in Fabrication, Structure, and Properties of Carbon Fibers, Polymer Reviews 52(3) (2012) 234-258.

[32] P.A. Manohar, M. Ferry, T. Chandra, Five Decades of the Zener Equation, ISIJ International 38(9) (1998) 913-924.

[33] S. Suarez, F. Lasserre, F. Mücklich, Mechanical properties of MWNT/Ni bulk

composites: Influence of the microstructural refinement on the hardness, Materials Science and Engineering: A 587 (2013) 381-386.

[34] L. Liu, W. Li, Y. Tang, B. Shen, W. Hu, Friction and wear properties of short carbon fiber reinforced aluminum matrix composites, Wear 266(7-8) (2009) 733-738.

[35] C.R. Carpenter, P.H. Shipway, Y. Zhu, The influence of CNT co-deposition on electrodeposit grain size and hardness, Surface and Coatings Technology 205(21-22) (2011) 5059-5063.

[36] J.Z. Lu, B. Han, C.Y. Cui, C.J. Li, K.Y. Luo, Electrochemical and pitting corrosion resistance of AISI 4145 steel subjected to massive laser shock peening treatment with different coverage layers, Optics & Laser Technology 88 (2017) 250-262.

[37] N. Dai, L.-C. Zhang, J. Zhang, X. Zhang, Q. Ni, Y. Chen, M. Wu, C. Yang, Distinction in corrosion resistance of selective laser melted Ti-6Al-4V alloy on different planes, Corrosion Science 111 (2016) 703-710.

[38] Z.H. Wen, Y. Bai, J.F. Yang, J. Huang, Corrosion resistance of vacuum re-melted Ni60-NiCrMoY alloy coatings, Journal of Alloys and Compounds 711 (2017) 659-669.

[39] N. Dai, L.-C. Zhang, J. Zhang, Q. Chen, M. Wu, Corrosion behavior of selective

laser melted Ti-6Al-4V alloy in NaCl solution, Corrosion Science 102 (2016) 484-489.

[40] Y. Yin, R.G. Faulkner, P. Moreton, I. Armson, P. Coyle, Grain boundary chromium depletion in austenitic alloys, Journal of Materials Science 45(21) (2010) 5872-5882.

[41] L. Liu, Y. Li, F. Wang, Influence of grain size on the corrosion behavior of a Ni-based superalloy nanocrystalline coating in NaCl acidic solution, Electrochimica Acta 53(5) (2008) 2453-2462.

[42] J. Qian, C. Chen, H. Yu, F. Liu, H. Yang, Z. Zhang, The influence and the mechanism of the precipitate/austenite interfacial C-enrichment on the intergranular corrosion sensitivity in 310 S stainless steel, Corrosion Science 111 (2016) 352-361.

[43] Y. Pan, G. Wu, Z. Huang, X. Wu, Y. Liu, H. Ye, Corrosion behaviour of carbon fibre reinforced polymer/magnesium alloy hybrid laminates, Corrosion Science 115 (2017) 152-158.

[44] D. Jun, L. Yao-hui, Y. Si-rong, L. Wen-fang, Dry sliding friction and wear properties of Al2O3 and carbon short fibres reinforced Al–12Si alloy hybrid composites, Wear 257(9-10) (2004) 930-940.

[45] Y. Tang, H. Liu, H. Zhao, L. Liu, Y. Wu, Friction and wear properties of copper

matrix composites reinforced with short carbon fibers, Materials & Design 29(1) (2008) 257-261.

[46] G. Garces, G. Bruno, A. Wanner, Load transfer in short fibre reinforced metal matrix composites, Acta Materialia 55(16) (2007) 5389-5400.

[47] P.B. Kadolkar, T.R. Watkins, J.T.M. De Hosson, B.J. Kooi, N.B. Dahotre, State of residual stress in laser-deposited ceramic composite coatings on aluminum alloys, Acta Materialia 55(4) (2007) 1203-1214.

[48] S. Zhou, X. Zeng, Q. Hu, Y. Huang, Analysis of crack behavior for Ni-based WC composite coatings by laser cladding and crack-free realization, Applied Surface Science 255(5) (2008) 1646-1653.

[49] F. Li, C.-B. Qu, Y. Hua, H.-M. Xiao, S.-Y. Fu, Largely improved dimensional stability of short carbon fiber reinforced polyethersulfone composites by graphene oxide coating at a low content, Carbon 119 (2017) 339-349.

[50] Kou, Sindo. Welding Metallurgy, Second Edition (2003) 253-280.

.

Figure captions

Fig. 1. (a) morphology of the composite powder and (b) the diameter distribution of the raw Ni-based powder.

Fig. 2. Schematic drawing of LC process

Fig. 3. XRD pattern in the 2θrange from 20°to 110°for Ni-based coating (A with laser scanning speed of 8 mm/s) and CFs/Ni coatings (B, C, D with laser scanning speed of 2 mm/s, 5 mm/s and 8 mm/s, respectively).

Fig. 4. The optical microscopy image of coatings. (a), (b) and (c) bonding zones, (e), (f) and (g) centre zones, and (i), (j) and (k) areas near top coating of the composite coating with laser beam scanning speed of 2 mm/s, 5 mm/s, 8 mm/s, respectively. (d), (h) and (l) microstructure of Ni-based alloy coating with laser scanning speed of 8 mm/s. (across-sections are made longitudinal to the laser beam scanning direction).

Fig. 5. High-magnified morphology of carbon fiber with laser scanning speed of (a) 2 mm/s and (b) 5 mm/s and (c) 8 mm/s, and (d) magnified morphology of B indicated in (c).

Fig. 6. EDS spectrum for the LMD-produced CFs/Ni-based composite coating at laser

scanning speed of 8 mm/s.

Fig. 7. TEM morphology of CFs distributed in coatings at laser scanning speed of (a) 2 mm/s and (b) 8 mm/s.

Fig. 8. (a) Microhardness of Ni-based coating and CFs/Ni-based coatings with laser scanning speed of 8 mm/s, and (b) the average microhardness of the composite coatings with different laser scanning speed, and (c) the relationship between the grain size d and the microhardness.

Fig. 9. The curves of electrochemical tests. (a) anodic polarization curves and (b) Nyquist plots and (c), (d) Bode plots.

Fig. 10. Morphology of the surface after electrochemical corrosion at 0.5 V for 20 min. (a) Ni-based coating with laser beam scanning speed of 8 mm/s and the composite coatings with laser beam scanning speed of (b) 2 mm/s, (c) 5 mm/s, and (d) 8 mm/s.

Fig. 11. High-magnified SEM image of the composite coating with laser scanning speed of 8 mm/s after corrosion.

Fig. 12. (a) friction coefficient and (b) wear rate of Ni-based coating and the composite coatings with friction process of 8h and the error lines represent the standard deviation.

Fig. 13. Morphology of the debris of (a) Ni-based coating with laser scanning speed of 8 mm/s and of the composite coatings with laser scanning speed of (b) 2 mm/s, (c) 5 mm/s, and (d) 8 mm/s.

Fig. 14. Morphology of the worn surface after the friction experiments. (a) surface of Ni-based coating with laser scanning speed of 8 mm/s and worn surfaces of the composite coatings with laser scanning speed of (b) 2 mm/s, (c) 5 mm/s, and (d) 8 mm/s.

Table captions

Table 1 Chemical composition of 1Cr13 substrate in wt.%.

Table 2 Chemical composition of Ni25 powder in wt.%.

Table 3 The physical properties of carbon fiber and nickel.

Table 4 Electrochemical parameters obtained from polarization curves of Ni-based alloy coating and the composite coatings.

Table 5 EDS analysis of the elements at different points in Fig. 13 and Fig. 14 (wt. %)。

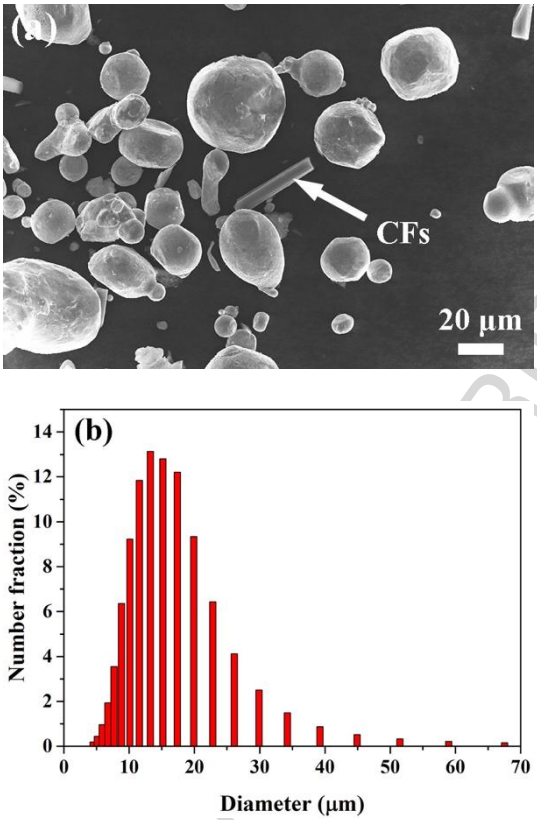

Fig. 1. (a) morphology of the composite powder and (b) the diameter distribution of the raw Ni-based powder.

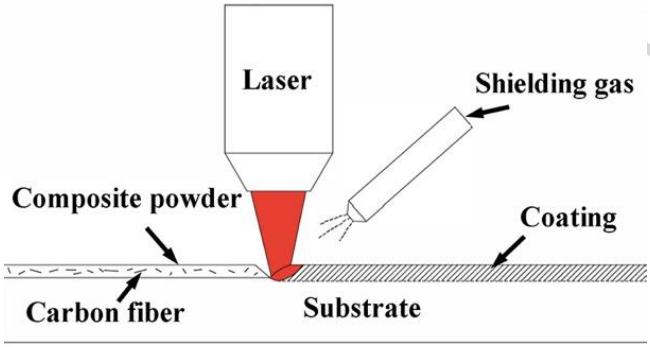

Fig. 2. Schematic drawing of LC process

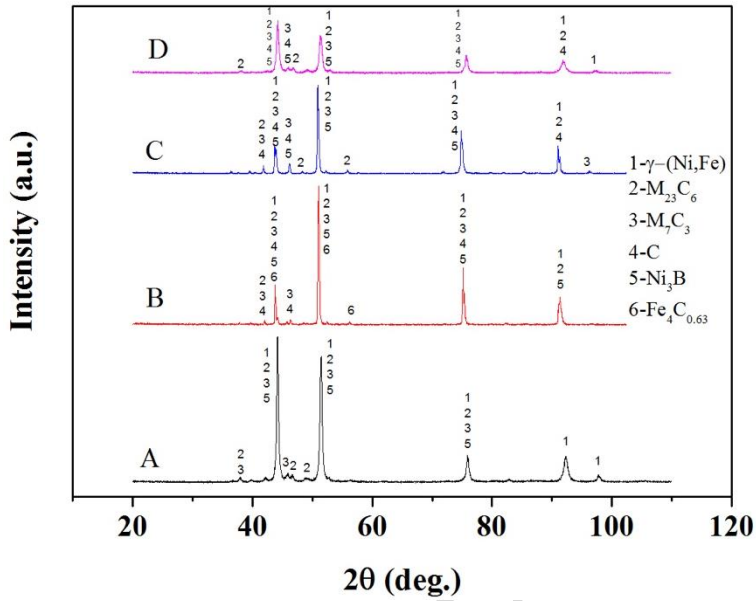

Fig. 3. XRD patterns in the 2θ range from 20° to 110° for Ni-based coating (A, with laser scanning speed of 8 mm/s) and CFs/Ni coatings (B, C, D with laser scanning speed of 2, 5, and 8 mm/s, respectively).

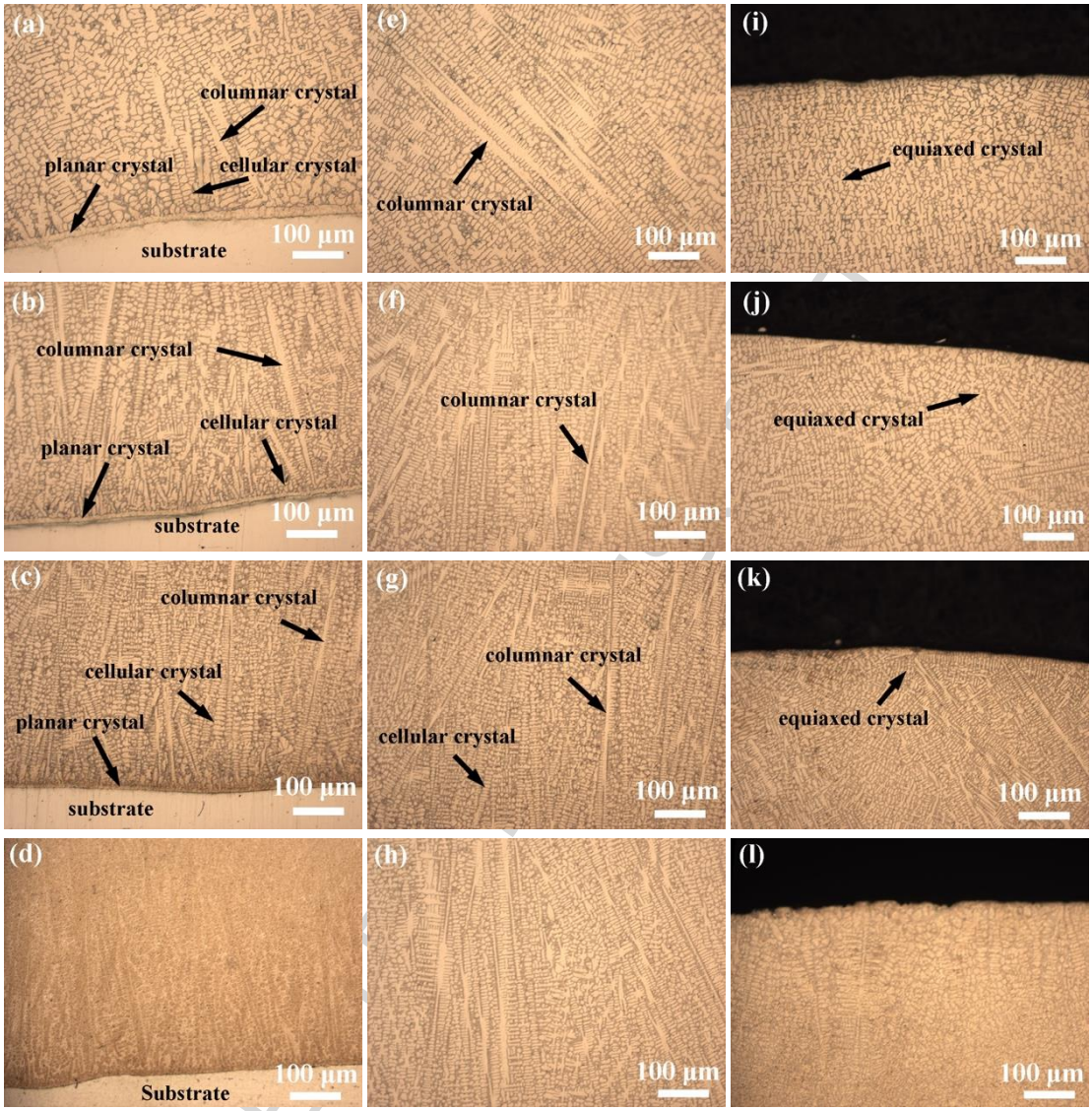

Fig. 4. The optical microscopy image of coatings: (a), (b) and (c) bonding zones, (e), (f) and (g) centre zones, and (i), (j) and (k) areas near top coating of the composite coating with laser scanning speed of 2 mm/s, 5 mm/s, 8 mm/s, respectively. (d), (h) and (l) microstructure of Ni-based alloy coating with laser scanning speed of 8 mm/s. (across-sections are made longitudinal to the laser scanning direction)

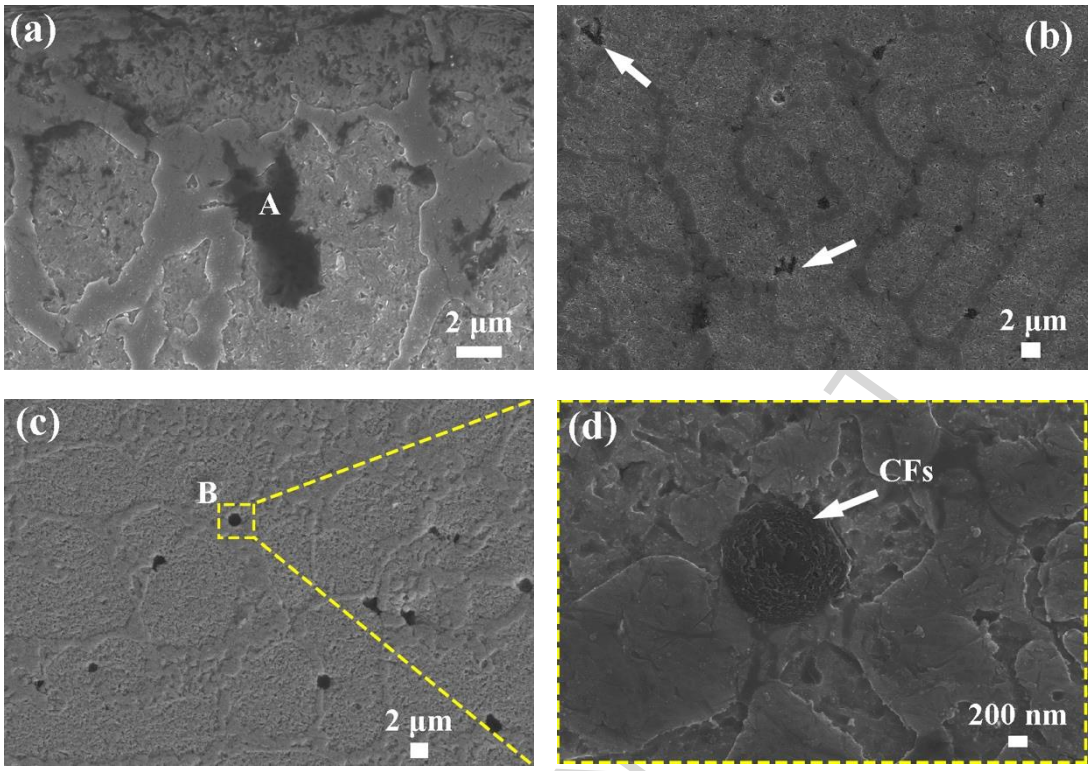

Fig. 5. High-magnified morphology of carbon fiber with laser scanning speed of (a) 2 mm/s, (b) 5 mm/s and (c) 8 mm/s, and (d) Magnified morphology of the region B indicated in (c).

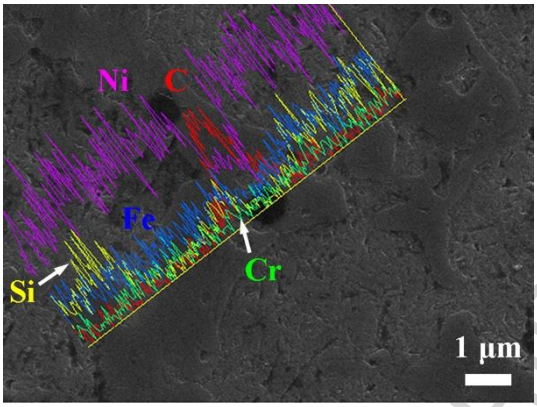

Fig. 6. EDS spectrum for the LMD-produced CFs/Ni-based composite coating at laser scanning speed of 8 mm/s.

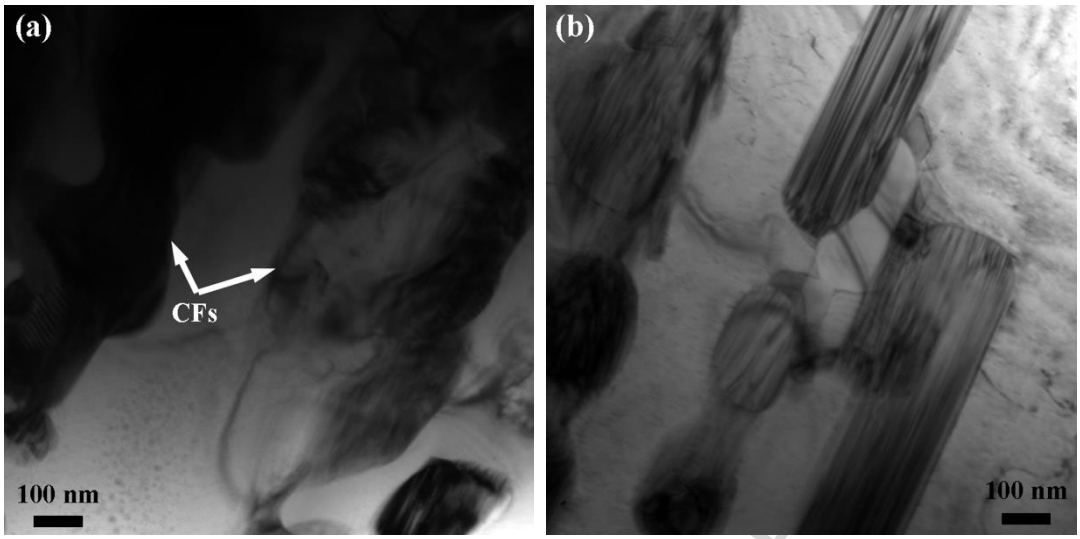

Fig. 7. TEM morphology of CFs distributed in coatings at laser scanning speed of (a) 2 mm/s and (b) 8 mm/s.

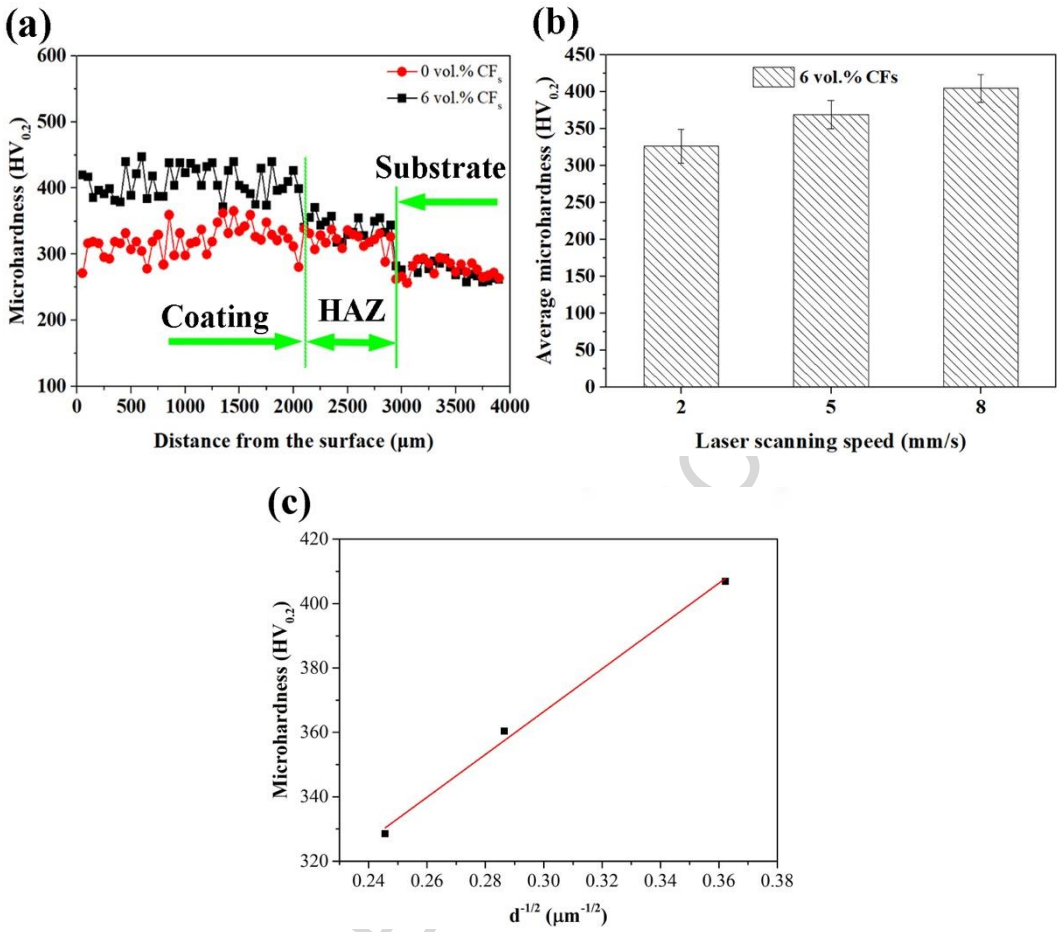

Fig. 8. (a) Microhardness of Ni-based coating and CFs/Ni-based coatings with laser scanning speed of 8mm/s, and (b) the average microhardness of the composite coatings with different laser scanning speed, and (c) the relationship between the grain size d and the microhardness.

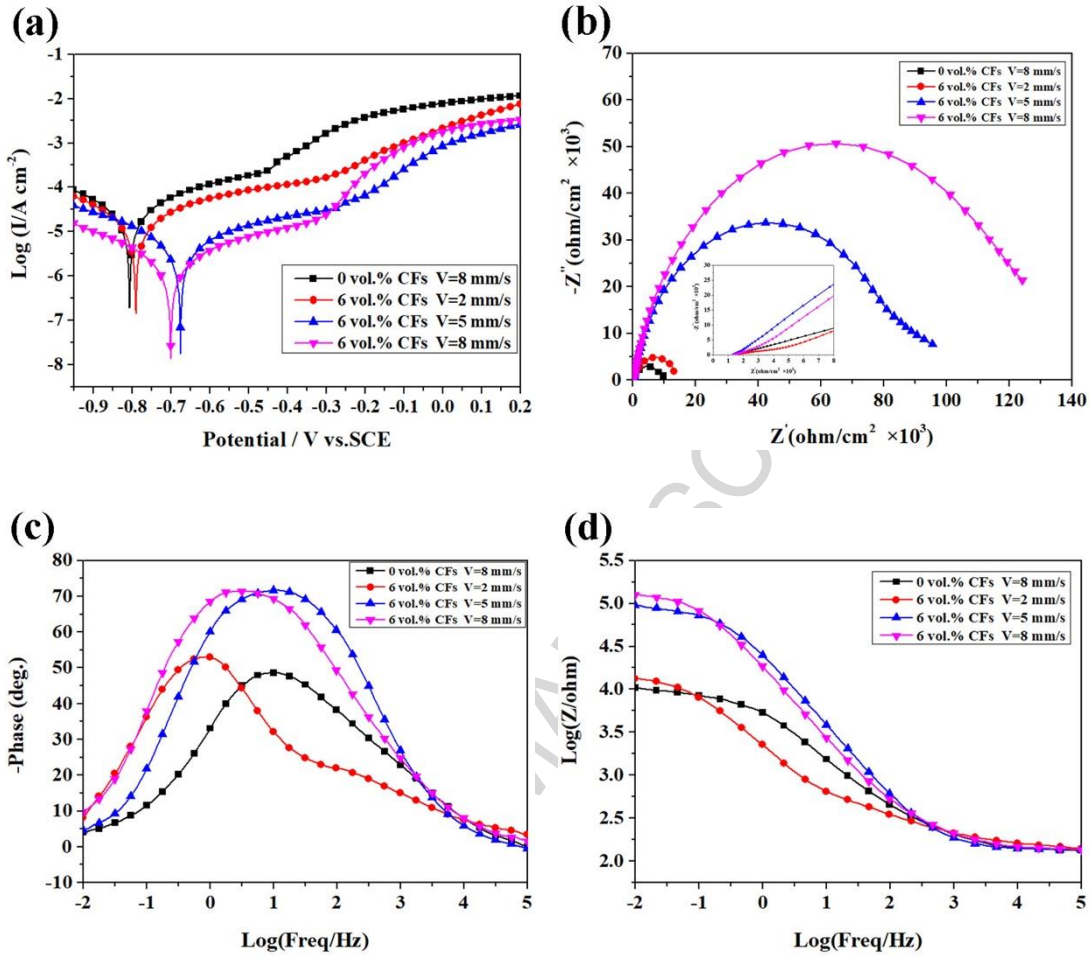

Fig. 9. The curves of electrochemical tests. (a) anodic polarization curves and (b) Nyquist plots and (c), (d) Bode plots.

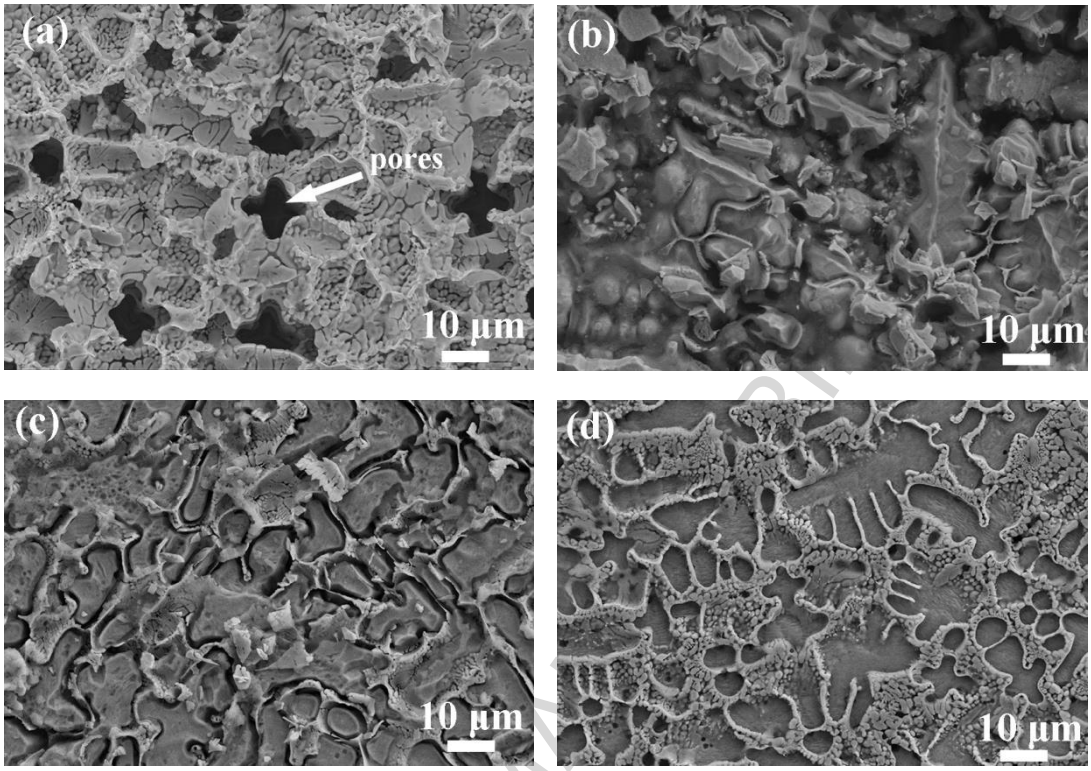

Fig. 10. Morphology of the surface after electrochemical corrosion at 0.5 V for 20 min. (a) Ni-based coating with laser scanning speed of 8 mm/s and the composite coatings with laser scanning speed of (b) 2 mm/s, (c) 5 mm/s, and (d) 8 mm/s.

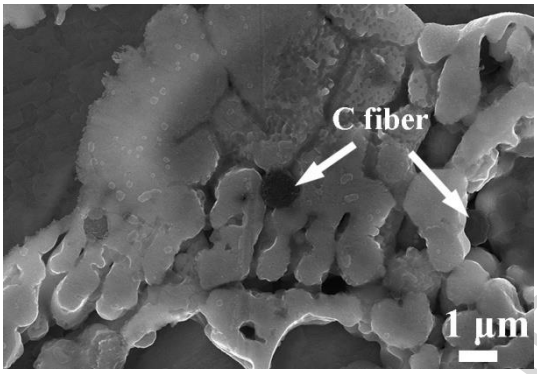

Fig. 11. High-magnified SEM image of the composite coating with laser scanning speed of 8 mm/s after corrosion.

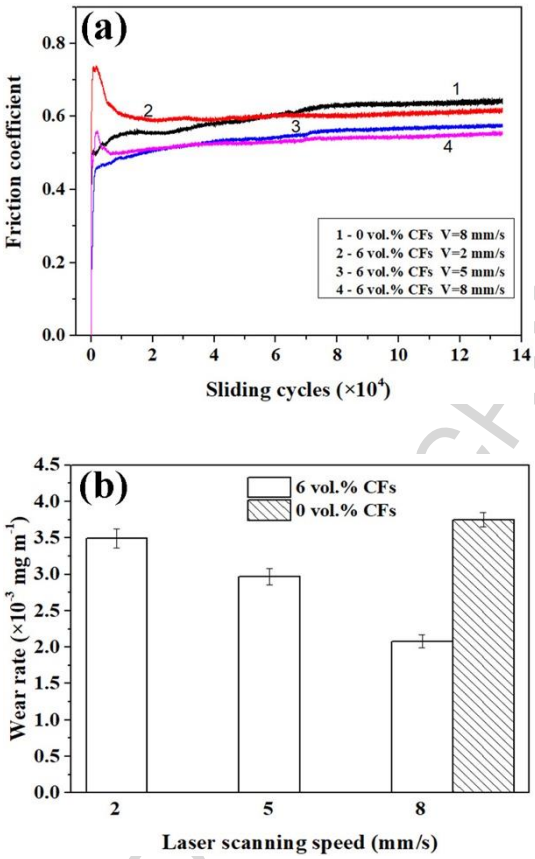

Fig. 12. (a) Friction coefficient and (b) wear rate of Ni-based coating and the composite coatings with friction process of 8h and the error lines represent the standard deviation.

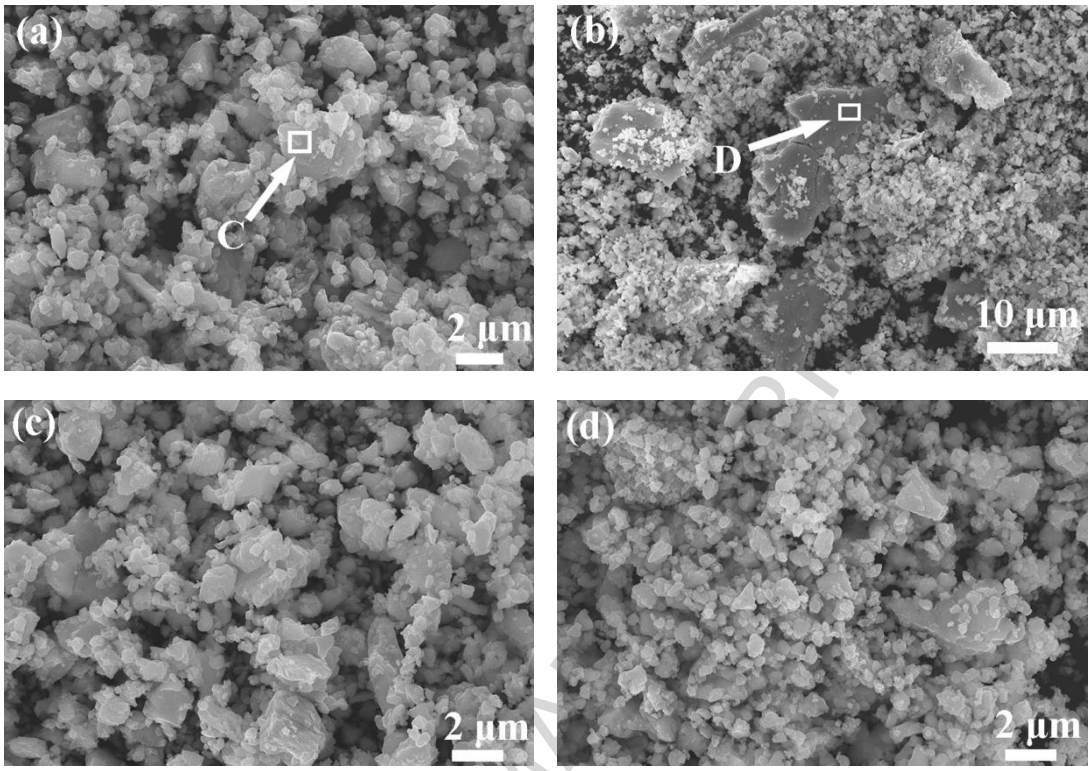

Fig. 13. Morphology of the debris of (a) Ni-based coating with laser scanning speed of 8 mm/s and of the composite coatings with laser scanning speed of (b) 2 mm/s, (c) 5 mm/s, and (d) 8 mm/s.

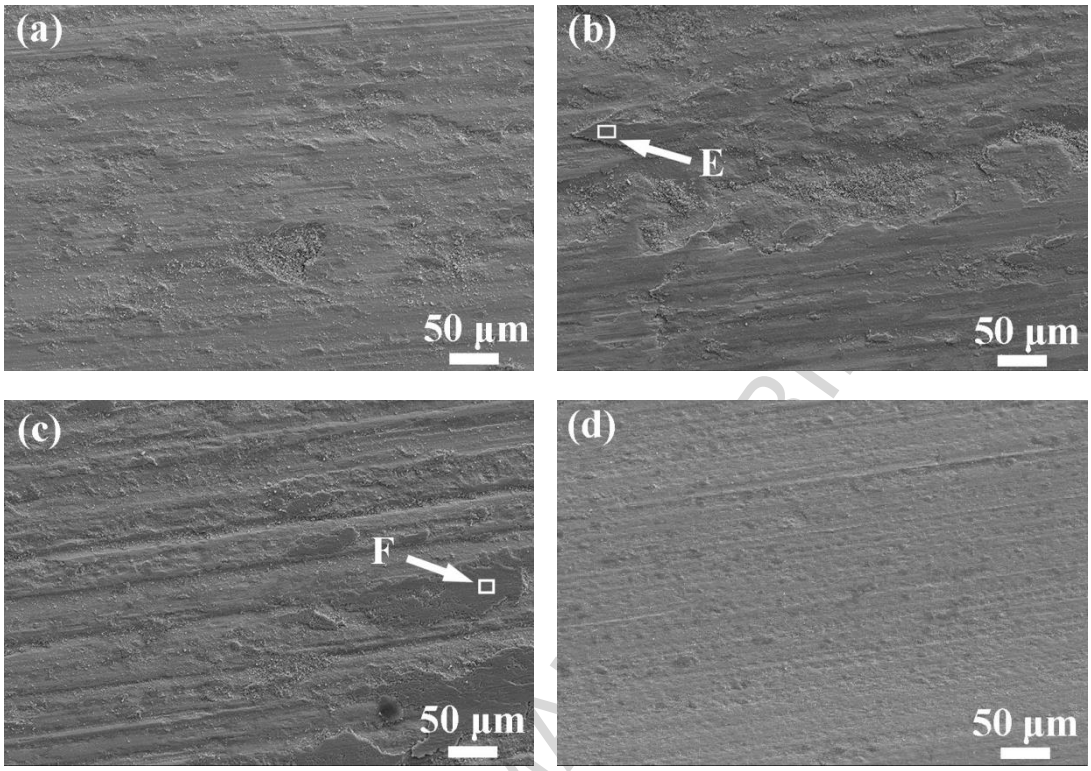

Fig. 14. Morphology of the worn surface after the friction experiments. (a) surface of Ni-based coating with laser scanning speed of 8 mm/s and worn surfaces of the composite coatings with laser scanning speed of (b) 2 mm/s, (c) 5 mm/s, and (d) 8 mm/s.

Tables

Table 1 Chemical composition of 1Cr13 substrate in wt.%.

Element	C	Mn	P	S	Si	Cr	Ni	Fe
Mass fraction	0.15	1	0.035	0.03	1	13.5	0.6	Bal.

Table 2 Chemical composition of Ni25 powder in wt.%.

Element	C	Cr	B	Si	Fe	Ni
Mass fraction	0.02	1.5	1	2.20-3.20	8.00	Bal.

Table 3 The physical properties of carbon fiber and nickel.

Samples	ρ g/cm^3	K W/(K·m)	C kJ/(kg·K)
C fiber	1.76	14	0.712
Ni	8.9	88.9	0.45

Table 4 Electrochemical parameters obtained from polarization curves of Ni-based coating and the composite coatings.

Samples		E_{corr} (V)	I_{corr} (A/cm^2)	R_p (ohm)	E_{pass} (V)	I_{pass} (A/cm^2)
0 vol.% CF_s	8mm/s	-0.806	2.350E-5	5745.7	-0.766	6.491E-5
	2mm/s	-0.790	1.406E-5	9688.8	-0.725	4.702E-5
6 vol.% CF_s	5mm/s	-0.675	3.789E-6	11141.7	-0.648	5.852E-6
	8mm/s	-0.701	1.663E-6	25350.3	-0.663	3.844E-6

Table 5 EDS analysis of the elements at different points in Fig. 13 and Fig. 14 (wt. %).

Point No.	C	O	Si	Cr	Fe	Ni
C	8.79	39.4	0.39	4.85	41.88	4.7
D	7.32	33.12	0.71	5.20	43.82	9.84
E	5.1	29.6	0.44	7.11	52.10	5.65
F	8.82	16.94	0.87	6.17	55.58	11.62

Highlights

1. Carbon fibers reinforced Ni-based composite coatings are fabricated by laser cladding.

2. Increasing laser scanning speed can improve the morphology and distribution of carbon fibers.

3. Carbon fibers can enhance the corrosion resistance and wear resistance of CFs/Ni-based coatings compared with Ni-based coating.

4. Corrosion and wear resistance of CFs/Ni-based coatings are further improved with increasing laser scanning speed.